Nano-genome editors accelerate mRNA cleavage through spatial confinement effect and reverse liver fibrosis by chemogene therapy

Jiayu Gu
China Pharmaceutical University
Jingfang Sun
China Pharmaceutical University
Kun Tian
China Pharmaceutical University
Jinlei Bian
China Pharmaceutical University
Juanjuan Peng
China Pharmaceutical University
Shu Xu
China Pharmaceutical University
Lingzhi Zhao (zlz@cpu.edu.cn)
China Pharmaceutical University https://orcid.org/0000-0002-3944-9716

Article

Keywords:

Posted Date: June 17th, 2022

DOI: https://doi.org/10.21203/rs.3.rs-1744036/v1

Abstract

Liver fibrosis is a chronic disease without effective treatment in the clinic. Gene editing systems such as the well-known CRISPR/Cas9 have shown great potential in the biomedical field. However, the delivery of the ribonucleoprotein is challenged by the large size of Cas9 (> 160 kDa) and the instable RNA probe. Recently, a structure-guided endonuclease (SGN) has been reported as an effectigene-editinging system composed of 35 kDa nuclease and stable DNA probes, which can regulate the protein expression by targeting specific mRNA outside the nucleus. Here, we conjugated the SGN to a nanomicelle as the delivery system. In the resulting material, the chance of the collision between the endonuclease and the probe was raised due to the confinement of the two components within the 40-nm nanomicelle, thus the mRNA can be cleaved immediately after being captured by the probe, resulting in a space-induced nucleotide identification-cleavage acceleration effect. The delivery system was used to treat liver fibrosis via the co-delivery of SGN and a drug rosiglitazone to the hepatic stellate cells, which separately downregulated the expression of tissue inhibitor of metalloprotease-1 and inactivated the hepatic stellate cells. The system successfully reversed the liver fibrosis in mice through the bidirectional regulatory that simultaneously promoted the degradation and inhibited the production of the collagen, demonstrating the great potency of the SGN system as gene medicine.

Introduction

Liver fibrosis is a global health problem characterized by the accumulation of extracellular matrix (ECM) as a result of repetitive liver damage, which can progress into liver cirrhosis, hepatic failure, and even hepatocellular carcinoma[1]. To date, no effective antifibrotic drug has been clinically approved[2]. The hepatic stellate cells (HSCs) have been identified as a potential target for antifibrotic therapy owing to their crucial involvement in the development and progression of liver fibrosis[3]. HSC is activated and converted into an α-smooth muscle actin (α-SMA)-expressing myofibroblast-like phenotype upon liver damage, resulting in liver tissue contraction and the production of ECM components such as collagen type I alpha 1 (collagen I)[4]. Most researches have focused on the inhibition of the collagen production[5–7]. However, the activated HSCs have not only increased collagen buildup, but also disrupted collagen degradation as a result of the overexpressed tissue inhibitor metalloproteinase 1 (TIMP1)[8]. Due to the complex pathogenesis, treatment with only a single modality may ameliorate but can hardly reverse the liver fibrosis[9].

Targeted genome editing by engineered nucleases has shown its great potential to heal chronic diseases[10]. Among the developed site-specific gene editing platform, the clustered regularly interspaced short palindromic repeats (CRISPR)-associated endonuclease (Cas9) is an available well-documented system[11–13]. The delivery of CRISPR/Cas9 is critical for the biomedical applications, which can be implemented in a variety of strategies, including the transfection by the Cas9-encoded plasmid DNA (pDNA)[14] or the delivery of the mRNA with the single guide RNA (sgRNA)[15]. Comparably, the direct delivery of the ribonucleoprotein (RNP) complex composed of the Cas9 protein and the sgRNA is more

favorable due to the merits of high efficiency, low off-target effects, low risk of deleterious gene mutation, low immunogenicity and the ease of production and storage[16–19]. As the delivery system, the non-viral synthetic nanoparticles have emerged as the safe and efficacious vehicles[20]. Gu et al.[21] prepared DNA nanoclews by the rolling circle amplification, and loaded the RNP of Cas9 protein and sgRNA on their surface through the binding affinity of DNA and RNA, which successfully disrupted the expression of enhanced green fluorescence protein (EGFP) in U2OS solid tumors on mice. Murthy et al.[22] assembled the Cas9 protein, gRNA and donor DNA on gold nanoparticles with thiolated DNA ligands for the gene therapy of Duchenne muscular dystrophy in mice through homology-directed repair. The CRISPR/Cas9 RNP were also loaded and delivered by the nanocarriers of metal organic frameworks[23], nanoparticles with arginine head-groups[24] and lipid-based nanoparticles[25, 26].

However, there are still several remaining challenges for the delivery of the CRISPR/Cas9 RNP, such as the high molecular weight of the Cas protein (> 160 kDa)[27], the instability of the sgRNA[28] and the requirement of the entrance to the nucleus[29]. Recently, a new structure-guided endonuclease (SGN)-based gene editing system consists of a flap endonuclease 1 (FEN1) plus hairpin DNA probe (hpDNA) was reported (HpSGN)[30]. Compared with CRISPR/Cas9, the HpSGN does not require the protospacer adjacent motif, thus can edit versatile gene targets of both DNA and RNA without sequence limitation. More importantly, the low molecular weight (~35 kDa) of the FEN1 protein and the stable hpDNA probe are beneficial for its *in vivo* delivery in the form of RNP, and the adoption of hpDNA allow the mRNA as cleaving targets, which can work outside the cell nucleus to avoid the difficulty of nucleus penetration[30, 31]. However, the *in vivo* delivery of HpSGN in the form of RNP has yet to be reported.

On the other hand, for the reversal of the liver fibrosis, combined therapies with elaborately designed targets are necessary[32–36]. For example, the bidirectional regulatory strategy for fibrosis that simultaneously inhibit collagen synthesis and promote collagen degradation has shown prominent antifibrosis effect[37, 38]. To this end, a nanocarrier capable of concomitant delivery of multiple active agents is required. We have prepared the silica cross-linked micelles (SCLMs) obtained by the self-assembly between triblock copolymer F108 (PEO_{132}–PPO_{50}–PEO_{132}, PEO represents polyethylene oxide, PPO represents polypropylene oxide) and silica species, which is composed of the surface polyethylene glycol (PEG) ligands from the PEO segments, a hydrophobic PPO core and an outside silica shell cross-linked the micelle[39]. The terminal groups of the F108 can be used as the modification sites of the RNP as guest molecules[40, 41], and the lipophilic core can accommodate the hydrophobic drugs[42]. Thus the SCLMs could serve as an ideal delivery system for the combined therapy.

Herein, we reported the reversal of the liver fibrosis on mice by the nanomedicine R@Hp-PSCLMs concomitantly deliver the RNP of HpSGN and the drug rosiglitazone using the SCLMs decorated with a targeting peptide as the nanocarrier. For the combined chemogene therapy, the FEN1 and the hpDNA probe were modified to the terminal groups of the surface PEG ligands for the RNP delivery, and the drug rosiglitazone was loaded inside the PPO core. Intriguingly, the *in vitro* RNA cleavage assay disclosed that the conjugation of the FEN1 and hpDNA probe to the adjacent polymer chains on the surface of the

SCLMs significantly improved the cleavage efficiency, which is due to the special confinement of the biomacromolecules within the 40-nm nanoparticle. For the targeted delivery to the activated HSCs, the peptide CTCE9908 was modified to SCLMs to enhance their specificity by the interaction with the overexpressed CXCR4[43]. After the endocytosis, the RNP cleaved the mRNA of *TIMP1* to promote the collagen degradation, and the rosiglitazone suppressed the proliferation and activation of HSCs to reduce the collagen production[44, 45]. Hence the accumulated collagen was scavenged by the bidirectional regulatory (Fig. 1). The *in vivo* experiments on ICR mice with liver fibrosis demonstrated that the combined chemogene therapy successfully downregulated the TIMP1 to upregulate the matrix metalloproteinase (MMP), promoted the expression of PPARγ to inactivate the HSCs, finally reversed the fibrosis and restored the liver function. This work provides a proof-of-concept study for the delivery of HpSGN as gene medicine on a nanocarrier with SINICA effect, which could be generalized as a platform for the treatment of chronic diseases with proper mRNA targets.

Results

Preparation and characterization of the nanocarrier. The obtained SCLMs prepared by the self-assembly between copolymer F108 and organic silica precursors. To provide the modification sites, maleimide groups (Mal) were modified to the terminal hydroxyl groups of F108 (Mal-F108-Mal), and the SCLMs with maleimides (Mal-SCLMs) were synthesized by mixing 7% of the Mal-F108-Mal in the F108 as the cosurfactant. The targeting peptide CTCE9908 was linked via the thioether bonds formed by the click reaction between the thiol groups on the cysteine and the Mal on SCLMs (PSCLMs). The probe HpDNA-SH with thiol group at the 5' end and the FEN1 thiolated by the Traut's reagent were attached to the PSCLMs through the same method to give the RNP-loaded SCLMs with targeting groups (Hp-PSCLMs). The obtained SCLMs, Mal-SCLMs, PSCLMs and Hp-PSCLMs were all monodispersed spherical nanoparticles with hollow structure (Fig. 1A) and similar size of 28 nm, their hydrated sizes measured by the dynamic light scattering (DLS) method were 39.6 ± 3.8 nm, 41.7 ± 3.8 nm, 41.6 ± 2.0 nm and 42.8 ± 2.0 nm with very low polydispersity index of ~ 0.15, respectively (Fig. 2B, S1). The larger hydrated size is due to the contribution of the PEG ligands. The zeta potentials of SCLMs, Mal-SCLMs and PSCLMs were similar, ranging from − 4.7 to -5.2 mV. The Hp-PSCLMs held a surface charge of -5.9 mV, which could be contributed to the modification of the negatively charged DNA probe and the FEN1 protein (Fig. S2). The nanocarrier exhibited good colloidal stability in biological fluids at least for 7 days (Fig. S3).

To verify the targeting capacity of CTCE9908, PSCLMs was labelled with Fluorescein Isothiocyanate (FITC, green) and the nuclei of HSCs were stained by 4', 6-diamidino-2-phenylindole (DAPI, blue). The HSCs were preincubated with transforming growth factor-β (TGF-β) for 24 h for the activation. As shown in Fig. 2C, HSCs incubated with FITC-labeled PSCLMs in serum-containing medium showed distinctively stronger green fluorescence than the FITC-labelled SCLMs without the targeting peptides, which can be attribute to the overexpressed CXCR4 on the cytomembrane of activated HSCs. In contrast, the preincubation of the free CTCE9908 saturated the receptors and inhibited the cellular uptake of the PSCLMs by the HSCs via the competitive inhibition effect. These results demonstrated that the ligand-

receptor interaction promoted the internalization of the nanocarrier into the HSCs, which could enhance the specificity of the nanocarrier in the fibrotic liver and achieve the targeted delivery in cellular level.

The *in vitro* release profile of rosiglitazone in PBS with 1% Tween 80 from the rosiglitazone-loaded PSCLMs (R@PSCLMs) showed a biphasic release pattern with an initial burst release of 76% rosiglitazone during the first 12 h followed by a slow and continuous release of 6% over the next 36 h (Fig. S4). To test the effect of rosiglitazone *in vitro*, the inhibitory rate of viability of R@SCLMs and R@PSCLMs was estimated by methyl thiazolyl tetrazolium (MTT) assay. Compared to the TGF-β treated group as control, both the R@SCLMs and R@PSCLMs inhibited the viability of the HSCs in a dose-dependent manner (Fig. S5). Specifically, the R@PSCLMs with targeting peptide resulted in a better inhibition effect at different concentrations, which demonstrated the benefit of the targeted delivery.

The accelerated mRNA cleavage of the nanosystem through spatial confinement effect. The cleavage efficiency of the HpSGN modified on the SCLMs was tested by denatured-polyacrylamide gel electrophoresis (PAGE). The targeted single-strand RNA (ssRNA) was modified with FAM at the 5’ end. To optimize the system, the FEN1 and hpDNA were modified on the SCLMs with different ratios of 9:1, 5:5 and 1:9, respectively, and the cleavage efficiency of free HpSGN with FEN1 to hpDNA ratio of 1:9 was also tested (Fig. 2D). From the statistical data in Fig. 2E, for the HpSGN conjugated on SCLMs, the FEN1 to hpDNA ratio of 1:9 afforded the highest cleavage rate of the targeted ssRNA under different concentrations. Upon the concentration with total FEN1 plus hpDNA of 0.5 μM, 97% of the substrate ssRNA was cleaved during 2 h. Therefore, the 1:9 was used for the loading ratio of the FEN1 and hpDNA on the nanocarriers. The cleavage efficiency between the free HpSGN and HpSGN modified on SCLMs in the optimized ratio of 1:9 was also compared. As shown in Fig. 2F, the free HpSGN is only effective at the concentration of 0.25 and 0.5 μM, while the conjugated HpSGN can still cleave ~ 18% of the ssRNA at a concentration as low as 0.06 μM. Intriguingly, the cleavage efficiency of the conjugated HpSGN was higher than the free HpSGN at all concentrations. Significantly, at the concentration of 0.5 μM, the cleavage efficiency of the conjugated HpSGN was 97%, and the ratio of the free HpSGN was only 55%. This accelerated mRNA cleavage is perhaps due to the spatial confinement of the endonuclease FEN1 and probe hpDNA within the 40-nm nanoparticle. Specifically, for the free HpSGN, the targeted loci can only be edited only if the FEN1, hpDNA and the substrate ssRNA randomly collide together, which hardly takes place in a highly diluted solution. Hence, as demonstrated, the free HpSGN did not work at low concentrations. However, upon the modification of the FEN1 and hpDNA on the SCLMs, the two molecules were limited in a confined space of 40 nm that fits the scale of the biomacromolecules, which shortens their distance and increases the collision chances. In other words, the modification on the SCLMs can be regarded as an “enrichment” of the FEN1 and hpDNA, thus improving the cleavage efficiency. We here define the phenomenon as space-induced nucleotide identification-cleavage acceleration (SINICA) effect. The anti-interference effect of the Hp-SCLMs was confirmed by a selective cleavage experiment. As shown in Fig. S6, with the proper hpDNA probe, the free HpSGN system (column 3) cleaved more than 40% of the substrate ssRNA-1, and the cleavage rate was improved to about 75% when the system was modified on SCLMs (column 4). With the addition of a free probe hpDNA-2

uncorrelated to the substrate, the cleavage efficiency for ssRNA-1 was not influenced (column 5), revealing good specificity and stability of the conjugated HpSGN system.

The biocompatibility of the nanoparticles was characterized before the *in vivo* assays. The nanocarrier showed good biocompatibility even at a high concentration of 400 $\mu g \cdot mL^{-1}$ in the MTT assay using HSC-T6 cells as model (Fig. S7). Hemolysis test revealed good blood compatibility in the blood of mice with less than 1% relative hemolysis rate at a high concentration up to 0.5 $mg \cdot mL^{-1}$ (Fig. S8). The *in vivo* toxicity test of histological analysis was shown in Fig. S9. No lesions can be found in the hematoxylin and eosin (H&E) stained tissue sections of the major organs such as heart, liver, spleen, lung and kidney after the systematically administration of the PSCLMs, Hp-PSCLMs through the tail vein at a dose of 40 $mg \cdot kg^{-1}$. The serological assay of ALT, AST, BUN and CRE indicated no significant difference between the control group and the treatment group, suggesting the SCLMs, PSCLMs, Hp-PSCLMs had no acute hepato- and nephrotoxicity (Fig. S10). These results demonstrated good biocompatibility of the nanocarrier with the RNP, assuring the safety for the animal experiment.

Biodistribution of the Hp-PSCLMs. It has been demonstrated that the SCLMs can be excreted through hepatobiliary pathway, which makes the nanoparticle passively accumulated in the liver. However, without active targeting ligands, the SCLMs were excreted rapidly and cannot be adequately retained at the lesion. Therefore, the peptide CTCE9908 targeting the overexpressed CXCR4 on the activated HSCs were modified to further enhance the liver accumulation specifically inside the targeted cells. The biodistribution of the Hp-PSCLMs was studied at the level of both organs and tissues, the Hp-SCLMs without the targeting peptide was used as the control. The organ distribution was determined using the covalently labelled Cy5.5 as tracer (Fig. 3A). The *ex vivo* imaging of the main organs showed that the fluorescence signal of Hp-SCLMs and Hp-PSCLMs from the liver of the subjected mice peaked at 12 h, and gradually decayed during 12–96 h. Comparing the two nanoparticles, the Hp-PSCLMs with the targeting peptide displayed obviously higher fluorescence at the liver, which is twice as much as the Hp-SCLMs in the first 48 h after injection (Fig. 3B), demonstrating the superior liver accumulation effect. Almost no accumulation of the nanoparticle was found at the other organs of heart, spleen, lung and kidney at the tested times, which validated the organ-specificity of the nanoparticle.

To locate the intrahepatic distribution of the nanoparticles, the α-SMA, as the biomarker for the activated HSCs, in the sections of the fibrotic liver was marked by immunofluorescence staining. As shown in Fig. 3C, the fluorescence of α-SMA (green) and Hp-PSCLMs (red) colocalized well in the merged image. The red fluorescence is overlapped or adjacent to the green fluorescence, which cannot be observed from the Hp-SCLMs group, confirming the SCLMs with CTCE9908 as targeting ligands can successfully be delivered the payloads to the HSCs.

The reversal of the liver fibrosis by the bidirectional regulatory chemogene therapy. The antifibrotic effect of the R@Hp-PSCLMs were tested in mice model with CCl_4-induced liver fibrosis (Fig. 4A). To attest the capability of the gene-editing system, the expression of the *TIMP1* mRNA in the fibrotic liver of the mice were determined by real-time quantitative PCR. As shown in Fig. 4B, by the 28-day of CCl_4 treatment, the

level of the *TIMP1* mRNA significantly elevated by about 31 folds relative to the control group (healthy mice). The direct intravenous administration of the free HpSGN system of the FEN1 and DNA probe showed almost no effect to inhibit the expression of the *TIMP1* mRNA, probably due to the lack of proper delivery vehicles. The NTHp-PSCLMs with the scrambled non-targeting hpDNA also failed to influence the mRNA level. In contrast, the Hp-PSCLMs carrying FEN1 plus hpDNA targeting the *TIMP1* remarkably suppressed the level of the mRNA, which was only one tenth as much as the fibrotic liver. The results demonstrated that the targeting nanocarrier PSCLMs successfully delivered the HpSGN to the activated HSCs, caught and cleaved the *TIMP1* mRNA, which could promote the expression of MMP to degrade the collagen.

The rosiglitazone and HpSGN system can act on different aspects for the pathogenesis of liver fibrosis to reduce the accumulation of collagen. Previous studies have demonstrated that the therapeutic effect was enhanced when two active agents were co-loaded in one nanocarrier, which ensured the agents were delivered concomitantly into the same cell to exert the synergistic effect. Thus, the better antifibrotic effect can be achieved in a combination therapy by integrating the rosiglitazone and HpSGN into a hybrid nanoparticle rather than delivering the two agents separately. The therapeutic efficacy of the nanomedicine R@Hp-PSCLMs with combined chemogene therapeutics was evaluated in the mice with CCl_4-induced liver fibrosis. The images of H&E and Masson trichome staining showed lobular architecture and little collagen deposition in the healthy liver, whereas the fibrotic liver sections manifested severe centrilobular necrosis, infiltration of lymphocyte and deposition of massive collagen fiber (Fig. 4C). The semi-quantitative analysis of the Masson trichome staining revealed that the liver treated by the combined chemogene therapy of the R@Hp-PSCLMs exhibited the least collagen accumulation (Fig. 4D). As the fibrotic liver showed a fibrotic area of 8.4 ± 0.2% of the total area, the treatment of R@Hp-PSCLMs dramatically reduced the area to 1.3 ± 0.2%, which is less than one sixth of the fibrotic liver and very close to the healthy liver (0.2 ± 0.07%). By contrast, the treatment with R@PSCLMs and Hp-PSCLMs can alleviate by failed to cure the fibrosis, showing a fibrotic area of 3.3 ± 0.4 and 4.5 ± 0.3%, respectively. Without the delivery system, the administration of the free rosiglitazone and free HpSGN reduced evidently less fibrosis, with the fibrotic area of 5.6 ± 0.6 and 6.6 ± 0.3%, respectively. The group treated by NTHp-PSCLMs, showed the fibrotic area of 7.3 ± 0.4%, which had no significant difference with the fibrotic mice. As the specific markers of liver fibrosis, the collagen I, α-SMA and TIMP1 were detected by immunohistochemistry or immunofluorescence. From Fig. 4C, it is obvious that except the control group, the largest and least brown area of collagen I was found from the fibrotic liver and the R@Hp-PSCLMs group. Similar results were observed from the green immunofluorescence indicating the expression of α-SMA and TIMP1. The quantitative data for the three markers were not quite the same but also similar to the fibrotic area, demonstrating the superiority of the bidirectional regulatory chemogene therapy mediated by the targeted nanocarrier (Fig. 4E-G).

The critical serological indexes liver function such as the alanine transaminase (ALT), aspartate transaminase (AST), and total bilirubin (T-BIL) and the hydroxyproline (Hyp) as the index for collagen were determined to evaluate the therapeutic efficacy (Fig. S11-14). All the indicators in the fibrotic group

were raised by at least 2 folds compared with the control group. For the treatment groups, the non-targeting treatment of free rosiglitazone and HpSGN showed no significant effect. In contrast, the targeted treatment using R@SCLMs, Hp-PSCLMs or R@Hp-PSCLMs significantly lowered the serum levels of ALT, AST, T-BIL and Hyp. Although the combined treatment only reduced the AST to a level close to the control group, and was unable to recover the levels of ALT, T-BIL and Hyp, the effect of the R@Hp-PSCLMs was still obviously better than the R@SCLMs and Hp-PSCLMs, indicating that the combined chemogene therapy did the best work to improve the liver function and alleviate fibrosis. The body weight of all the groups of the mice increased steadily in a similar rate during the 4-week treatment, showing no obvious side effect that influence the weight of the mice (Fig. S15).

The expression of some fibrosis-related proteins was analyzed and shown in Fig. 5. The results for the expression of collagen I, α-SMA, and TIMP1 obtained by the western blot analysis are in line with the histological and immunofluorescence staining images. The three upregulated proteins in the CCl_4-treated mice were barely inhibited by the non-targeting treatment of free rosiglitazone, free HpSGN, and the NTHp-PSCLMs with the scrambled hpDNA sequence. In contrast, the treatment by R@PSCLMs, Hp-PSCLMs and R@Hp-PSCLMs significantly downregulated the expression of collagen I, α-SMA, and TIMP1, and the R@Hp-PSCLMs exhibited the best performance.

Among all the antifibrotic treatments, the direct inhibition of the activation and proliferation of HSCs is the most direct and effective method owing to its function for collagen deposition. In the antifibrotic treatment, the drug rosiglitazone plays a role of the agonist for PPARγ to inhibit the activation and proliferation of HSCs. The level of PPARγ in the CCl_4-treated group notably decreased, indicating massive activated HSCs in the chronic liver injury. The level of PPARγ was significantly raised by the targeted drug delivery of the R@PSCLMs and R@Hp-PSCLMs compared with free rosiglitazone (Fig. 5A, E). The Hp-PSCLMs also increased the PPARγ to some extent, which may due to the deactivation of the HSCs by the reduced collagen[46]. The MMP family is responsible for the degradation of extracellular matrix, which is crucial for the clearance of the scar tissue in the fibrotic liver. The TIMP1 can specifically bind to the zinc in the catalytic center of MMP1 through its N-terminal to block its catalytic activity. As shown in Fig. 5A, F, in the treatment groups of Hp-PSCLMs, and R@Hp-PSCLMs with the inhibited expression of TIMP1, the expression of MMP1 was recovered by the targeted delivery of the HpSGN, especially in the combined therapy.

The *in vivo* experiment revealed good antifibrotic capacity of the combined chemogene therapy. It is also demonstrated that the PSCLMs as the delivery system successful send the HpSGN to the HSCs in the form of RNP, efficiently cleaved the targeted mRNA, and helped to cure the chronic liver fibrosis.

Discussion

Gene therapy has been regarded as a promising candidate for various intractable diseases. Many classical gene editing nucleases, including zinc-finger nucleases (ZFNs)[47], transcription-activator-like effector nucleases (TALENs)[48] and CRISPR-associated systems[49] have been explored to date. The ZFNs

and TALENs depend on the recognition of specific sequences by programmable protein-DNA interactions. Hence, a laborious process is required to engineer the specific protein to recognize each targeted DNA sequence. The famous site-specific gene editing platform, CRISPR/Cas, is one of the universal genome editing machineries which can be guided by a short RNA molecule to the targeted genomic DNA[50]. The delivery of the CRISPR/Cas system is critical for the biomedical applications, which can be implemented in several patterns, including the Cas-encoded pDNA, mRNA or RNP. However, the off-targeted pDNA or mRNA could lead to the expression of the Cas protein in the undesired cells, and even the expression in the targeted cell is hardly controllable, leading to unknown risks. As the made-up equipment that does not rely on transcription or translation, the delivery of the RNP composed of the Cas protein and the sgRNA is the most direct and rapid method, and often the preferential choice for CRISPR/Cas gene editing *in vivo*[51]. The large size of the Cas9 protein and the instability of the sgRNA bring about difficulties to the CRISPR/Cas RNP delivery. Fortunately, the recently reported HpSGN system is an ideal alternative that consists of the protein FEN1 with only 35 kDa plus a probe hpDNA, which could edit both DNA and RNA without the sequence limitation from the protospacer adjacent motif.

As for the delivery vehicle, despite of the effectiveness of the viral vectors, they present several drawbacks including restrictive packaging limits, risk of random deleterious integration into the genome, and potential immune response[52]. For the non-viral vectors, the nanoparticle-based carriers emerged as a safe and efficacious approach without the packaging restrictions[53]. In addition, the nanocarriers can be engineered with targeting ligands to precisely deliver the payloads to the aimed organs[54], cells[55] or even subcellular organelles[56]. For the delivery of the RNP of HpSGN, the SCLMs was used as a safe and efficacious non-viral system. Interestingly, we found that the special confinement of the RNP within the 40-nm nanoparticle by the decoration of the FEN1 and hpDNA onto the surface PEG ligands of SCLMs dramatically improve the gene editing efficiency, which perhaps due to the increased probability of the molecular collision between the FEN1 protein and the hpDNA/mRNA complex.

Liver fibrosis is a chronic disease without effective therapeutic approach in the clinic to date. Due to its complicated pathogenesis, an elaborated therapeutic cocktail is usually more effective than a single treatment. Here, the gene therapy was combined with the chemo therapy to simultaneously improve the degradation and inhibit the production of collagen. To improve the specificity of the therapy, CTCE9908 was conjugated on the surface of SCLMs to target the activated HSCs, which is considered as the culprit for the collagen deposition in the fibrotic process. The animal experiment revealed remarkably alleviated liver fibrosis and recovered liver functions, demonstrating not only the good antifibrosis effect of the combined therapy but also the capacity of the HpSGN system *in vivo*. The methodology is envisioned to be applied to other illnesses such as cardiovascular or genetic diseases by the precise manipulation of the key gene associated to the disorders.

Methods

Materials. Pluronic surfactant F108, cyclohexane, tetraethyl orthosilicate (TEOS), diethoxydimethylsilane (DEDMS), dimethyl sulfoxide (DMSO), carbon tetrachloride (CCl_4), corn oil, rosiglitazone were purchased from Sigma-Aldrich. Near-infrared fluorescent dye Cy5.5-NHS ester was purchased from Lumiprobe Corporation. Rat HSC cell line (HSC-T6) was purchased from the Procell Life Sciences&Technology Co, Ltd. CTCE9908 peptide (sequence: Lys-Gly-Val-Ser-Leu-Ser-Tyr-Arg-Cys-Arg-Tyr-Ser-Leu-Ser-Val-Gly-Lys) were purchased from Nanjing Peptide Industry Biotechnology Co., Ltd. Male ICR mice (20 ± 2 g) were obtained from the Animal Centre of Yangzhou University.

Synthesis of SCLMs, PSCLMs, Hp-PSCLMs. Briefly, Pluronic copolymer F108 (0.25 g) was dissolved in aqueous HCl solution (7.5 mL, 2.0 M) under vigorous stirring at room temperature. Then, cyclohexane (240 μL) was added and dispersed by sonication, and the emulsion was stirred for another 30 min. Afterwards, TEOS (268 μL) was added and stirred for 4 h at room temperature before the addition of DEDMS (120 μL). 24 h later, the product was dialyzed in deionized water for 5 times (20 000 Da molecular weight membrane) to purify the product. Cyclohexane was removed at by rotary evaporation at 50°C under 150 mbar for 15 min. To remove the potential precipitates, the product was centrifuged at 5000 rpm for 15 min and the supernatant with SCLMs was filtered by a 0.22 μm membrane before the characterization and applications.

Mal-F108-Mal was synthesized as described by Frayne et al[57] (Fig. S16). Furan (1.05 g) and maleimide (1 g) were dissolved in diethyl ether (15 mL) in a sealed tube, and heated for 12 h at 100°C. After cooling down to room temperature, the precipitiation was filtered, washed with diethyl ether and dried to afford compound 1 (Fig. S17). 1H NMR (300 MHz, DMSO) δ 11.15 (s, 1H), 6.53 (s, 2H), 5.11 (s, 2H), 2.85 (s, 2H). F108 (7.3 g, 0.5 mmol) and *p*-toluenesulfonyl chloride (0.955 g, 5 mmol) was dissolved in tetrahydrofuran (100 mL). The aqueous solution of sodium hydroxide (0.8 g, 10 mmol) was slowly added to the solution under stirring. The resulting mixture was warmed to 50°C and stirred overnight. After the reaction, the mixture was concentrated under reduced pressure and the solid was dissolved in dichloromethane. The organic layers were washed with water and saturated saline solution, then dried by anhydrous sodium sulfate. The solvent was evaporated to afford the crude product Ts-F108-Ts (Fig. S18). 1H NMR (300 MHz, D_2O) δ 7.79 (d, J = 7.7 Hz, 4H), 7.46 (d, J = 7.8 Hz, 4H), 3.63 (s, 1471H), 3.49 (dt, J = 13.4, 6.7 Hz, 457H), 2.40 (s, 6H), 1.20–0.99 (m, 637H). Compound 1 (0.33 g, 2 mmol) and Ts-F108-Ts (2.92 g, 0.2 mmol) were dissolved in acetone, potassium carbonate (0.278 g, 2 mmol) was then added, the mixture was refluxed for 60 hours under an inert N_2 atmosphere. After completion, the solids were removed by filtration and the filtrate was concentrated under reduced pressure to afford compound 2 (Fig. S19). 1H NMR (300 MHz, D_2O) δ 6.64 (s, 4H), 5.32 (s, 4H), 3.72 (s, 1416H), 3.63–3.43 (m, 131H), 3.14 (s, 5H), 1.18 (d, J = 5.7 Hz, 179H). Compound 2 (3 g, 0.2 mmol) was dissolved in toluene (20 mL) and refluxed under an inert N_2 atmosphere overnight. The solvent was removed and the residue was dissolved in 20 mL dichloromethane, the mixture was added dropwise to stirred diethyl ether. The precipitation was collected and washed with diethyl ether repeatedly, then dried under high vacuum to afford Mal-F108-Mal (Fig. S20). 1H NMR (300 MHz, D_2O) δ 6.93 (s, 2H), 3.75 (s, 1190H), 3.61 (d, J = 4.9 Hz, 102H), 1.21 (d, J = 5.9 Hz, 150H)

In the synthesis of Mal-SCLMs, Mal-F108-Mal was doped in F108 in a weight ratio of 7% (0.0175 g Mal-F108-Mal and 0.2325 g F108), and solubilized in HCl (7.5 mL, 2.0 M). The next steps are the same as the above synthetic method of SCLMs to obtain Mal-SCLMs. PSCLMs was obtained through the click reaction between the sulfhydryl group of CTCE9908 peptide and maleimide group. CTCE9908 (1.8 mg) was then added to Mal-SCLMs and stirred at room temperature for 2 h. The solution was collected and dialysis in deionized water for 5 times (20 000 Da molecular weight membrane) to remove the excessive reactants and impurities. Then the solution was centrifuged at 5000 rpm for 10 min, and the supernatant was filtered using a 0.22 μm filter to obtain PSCLMs. The concentration of SCLMs and CT-SCLMs was determined by lyophilization.

The sulfhydryl group was modified to FEN1 by Traut's reagent to obtain FEN1-SH. HpDNA-SH was synthesized by the modification of the 5'-end of the strand of hpDNA with the sulfhydryl group. FEN1-SH (400 pmol) and hpDNA-SH (3600 pmol) were added to SCLMs (0.78 mg) and reacted at room temperature for 2 h. The product was denoted as Hp-SCLMs with a ratio of FEN1 to hpDNA of 1:9. Hp-PSCLMs was synthesized in the same method using the PSCLMs as substrate.

Characterizations. Transmission electron microscopy (TEM) images were captured on a JEOL JEM-1400 transmission electron microscope with operation voltage of 100 kV. Dynamic light scattering (DLS) and zeta potential experiments were performed at 25°C using an Anton Paar Litesizer 500 nm particle size analyzer. Absorption spectra were obtained by a Philes G9-9S Uv-visible spectrophotometer. Confocal images of cells and tissues were recorded on an Olympus FV3000 Confocal Laser Scanning Microscope (CLSM).

In vitro **RNA cleavage assay.** A 10 μL mixture consisting of single-strand RNA (ssRNA) substrate (10 pmol) (see Table S1 for the sequence), 3-(4-Morpholino) propanesulphonic acid (10 mM), 0.05% Tween-20, 0.01% nonidet P-40, $MgCl_2$ (7.5 mM), and Hp-PSCLMs (1 μg) with designed ratio of hpDNA and FEN1 was incubated at 37°C for 2h. The 5'-end of the target ssRNA was modified with fluorescent FAM. The products were analyzed by denatured-polyacrylamide gel electrophoresis (PAGE) under denaturing conditions. The loading buffer contained 90% formamide, 0.5% EDTA, 0.1% xylene cyanol, and 0.1% bromophenol blue. Before loading, 10 μL loading buffer was added to the 10 μL reaction mixture. The sample was then loaded onto a 20% PAGE gel at room temperature for the electrophoresis in a buffer containing urea (8.7 M) and triborate (89 mM) with a speed of 9.6 $V \cdot cm^{-1}$ for 2 h. The gel was imaged by an Amersham Imager 600 (GE Healthcare). The protocol of the cleavage using the Hp-SCLMs was the same as the above method using free HpSGN.

Loading of rosiglitazone. Rosiglitazone was dissolved in DMSO to form a solution with a concentration of 100 $mg \cdot mL^{-1}$. Then, the 10 μL DMSO solution containing rosiglitazone were added to a solution with the drug carriers (20 $mg \cdot mL^{-1}$) under vigorous sonication to load the hydrophobic molecules into the PPO core of SCLMs. The rosiglitazone-loaded drug carriers were denoted as R@SCLMs, R@PSCLMs and R@Hp-PSCLMs, respectively. The loading ratio of rosiglitazone was determined by UV-vis as 5%.

In vitro **release of rosiglitazone.** The release rate of rosiglitazone was monitored under sink conditions in a PBS solution (pH 7.4) with 1% Tween 80. The drug carrier (5 mL, 4 mg·mL^{-1}) containing rosiglitazone (0.2 mg·mL^{-1}) was sealed in a dialysis membrane with MWCO of 8000–14000. The dialysis bag was then soaked in PBS (45 mL) at 37°C with constant stirring (120 rpm). At designed time, 1 mL of the release medium was withdrawn and replaced with the same amount of fresh PBS with 1% Tween 80. The released amount of the drug was determined by UV-absorption using a PHILES G-9S ultraviolet spectrophotometer.

Cell culture. HSC-T6 rat hepatic stellate cells were cultured in DMEM supplemented with 10% FBS. All cells were incubated at 37°C in a humidified 5% CO_2 atmosphere.

Toxicity Studies. The *in vitro* cytotoxicity of the nanocarriers were investigated by MTT assay. HSC-T6 cells were seeded to a 96-well plate (1 × 10^4 cells per well) and cultured overnight at 37°C in 200 μL medium containing 10% FBS. Then the DMEM medium in the plate was replaced by 200 μL FBS-free medium containing different concentrations of the drug carrier (0, 3.125,6.25,12.5,25, 50, 100, 200 and 400 μg·mL^{-1}), and the cells were incubated for another 24 h. Afterwards, 20 μL MTT solution (5 mg·mL^{-1}) was added to each well in the 96-well plate and the plates were further incubated at 37°C for 4 h in the dark. After that, the medium was removed and 150 μL dimethyl sulfoxide (DMSO) was added to each well to dissolve the formazan crystals. The plate was shaken gently on the shaker at room temperature for 15 min. Cell viability was estimated based on the absorbance at 570 nm in each well. Cell viability was calculated according to the following formula:

$$\mathrm{Cellviability}(\%) = \frac{Abs^{treatment}}{Abs^{control}} \times 100\%$$

The biosafety of PSCLMs and Hp-PSCLMs were further tested *in vivo*. The mice were intravenously injected with PSCLMs or Hp-PSCLMs (4 mg·mL^{-1}, 200 μL) or saline for 24 h then the mice were sacrificed and the main organs (heart, liver, spleen, lung, and kidney) were harvested for H&E staining. The blood were collected for the ALT, AST, CRE, BUN test using commercial test kits (Jiancheng BioTech, Nanjing, China).

Hemolytic activity study. Hemolytic activity was evaluated using the blood from mice. Different concentrations of SCLMs, PSCLMs and Hp-PSCLMs (0.05, 0.1 and 0.5 mg·mL^{-1}) were incubated with 2% red blood cell suspension at 37°C for 3 h. Blood (200 μL) mixed with saline and distilled water served as negative and positive controls, respectively. Following, all samples were centrifuged at 680×g for 5 min and the supernatant was added to a 96-well plate to measure the absorbance at 540 nm. The calculation of hemolysis rate is as follows:

$$\mathrm{Hemolysisrate}(\%) = \frac{Abs - Abs^{negativecontrol}}{Abs^{positivecontrol} - Abs^{negativecontrol}} \times 100\backslash\%$$

In vitro **inhibitory effect of rosiglitazone on cell proliferation.** HSC-T6 cells were seeded in 96-well plates at a density of 1×10^4 cells per well and cultured for 12 h. Then the medium was removed and cells were incubated for 24 h with fresh medium containing 10 ng·mL^{-1} TGF-β to activate HSCs. The fresh medium was replaced with the medium containing different concentrations of R@SCLMs or R@PSCLMs (with rosiglitazone of 1.56, 3.13, 6.25, 12.5, 25.0 and 50.0 μg·mL^{-1}) for another 24 h before the MTT assay. The group with no treatment was used as a control. The calculation formula of the inhibitory rate of cell proliferation is as follow:

$$\mathrm{Inhibitoryrateofcellproliferation}(\%) = \frac{Abs^{Control} - Abs}{Abs^{Control}} \times 100\%$$

In vitro **cellular uptake analysis of PSCLMs.** HSCs were seeded in confocal dishes at a density of 5×10^3 cells per dish and incubated in 1 mL of DMEM supplemented with 10% FBS for 12 h. Then the cells were incubated for 24 h with fresh medium containing 10 ng·mL^{-1} TGF-β to activate HSCs. Activated HSCs were treated with SCLMs or PSCLMs loaded with FITC (100 μg·mL^{-1}). For the free ligand competitive inhibition assay, the CXCR4 on the activated HSCs were saturated by free CTCE9908 (50 μg·mL^{-1}) for 30 min before incubation with FITC-labeled PSCLMs. 4 h after the addition of the drug carriers, the cells were washed three times with PBS and fixed with 4% paraformaldehyde for 30 min at room temperature. Afterwards, the cells were washed three times with PBS and stained with DAPI for 10 min. Finally, after washed with PBS for three times, the fluorescence of FITC and nuclei was observed by confocal laser scanning microscopy.

Animal models of liver fibrosis. Six-week-old male ICR mice (20 ± 2 g) were obtained from the Animal Centre of Yangzhou University (Yangzhou, China). All animal experiments were conducted under protocols approved by the Ministry of Health of the People's Republic of China and following Guidelines for the Care and Use of Laboratory Animals of China Pharmaceutical University (2022-04-001). All mice were housed at 25°C at 40–60% humidity. Liver fibrosis was induced by CCl_4 in ICR mice. CCl_4 and corn oil mixture (1:9 in volume ratio) was given by intraperitoneal injection twice a week for 4 weeks (at the 1st, 4th, 8th, 11th, 15th, 18th, 22nd, 25th day) at a dose of 10 mL·kg^{-1}.

Biodistribution and intrahepatic distribution of nanoparticles. For the biodistribution study, the fibrotic mice were administered with a single intravenous injection of the nanoparticles prepared with Cy5.5-labeled Hp-SCLMs or Hp-PSCLMs (4 mg·mL^{-1}, 200 μL). The fluorescence signals of the main organs (heart, liver, spleen, lung, and kidney) were monitored and analyzed at 2, 12, 24, 48 and 96 h after injection using a Vilber FUSION FX7 imaging system (λ_{ex} = 680 nm, λ_{em} = 750 ± 10 nm).

For the intrahepatic distribution, the mice were sacrificed 24 h after the injection of the drug carriers (4 mg·mL^{-1}, 200 μL) and the liver tissues were sectioned for immunofluorescence staining. α-SMA was stained with an anti-α-SMA antibody and a 488-conjugated secondary antibody to label activated HSCs. Nuclei were stained with DAPI. Immunofluorescence images were captured using a CLSM.

Therapeutic efficacy. The liver fibrosis mice were established by the aforementioned method. During the 4-week administration of CCl_4, the mice were intravenously injected with 200 μL of 4 $mg{\cdot}mL^{-1}$ NTHp-PSCLMs, R@PSCLMs, Hp-PSCLMs and R@Hp-PSCLMs (at the 16th, 19th, 23nd, 26th day). As negative control, the free rosiglitazone (2 $mg{\cdot}kg^{-1}$, 200 μL) and HpSGN (4 nmol per mice) were also injected intravenously to another two groups of mice at the same time. The concentrations of rosiglitazone and HpSGN in the drug carriers were the same as the negative control groups. The body weights of the mice were recorded. Afterwards, all the mice were sacrificed, the liver and blood were harvested for further analysis.

The levels of ALT, AST and T-BIL in blood and hydroxyproline (Hyp) in the liver were determined using analysis kits according to the manufacturers' instructions (Nanjing JianCheng Bioengineering Institute, China). H&E and Masson were stained according to the standard histological procedures. Protein expression of collagen I, α-SMA, TIMP-1, PPARγ and MMP1 in liver after different treatments were measured by western blot and the bands were analyzed by ImageJ. The expression of TIMP1 and α-SMA were determined by immunofluorescence and the fluorescence were quantified by ImageJ. The expression of collagen I was determined by immunocytochemistry and their positive areas were analyzed using ImageJ. The level of TIMP1 was analyzed by qPCR and the sequences of the primers were shown in Table S2.

$$\mathrm{Cellviability}(\%) = \frac{\mathrm{meanAbsvalueoftreatmentgroup}}{\mathrm{meanAbsvalueofcontrolgroup}} \times 100\%$$

Statistical analyses. All data are presented as the mean ± standard deviation obtained from at least three independent experiments. The two-tailed Student's t-test was used to compare the data in two groups. $P < 0.05$ was considered significant.

References

1. Kisseleva, T. & Brenner, D. Molecular and cellular mechanisms of liver fibrosis and its regression. Nat. Rev. Gastroenterol. Hepatol. **18**, 151–166 (2021).
2. Santoro, R. & Mangia, A. Progress in promising anti-fibrotic therapies. Expert Rev. Gastroenterol. Hepatol. **13**, 1145–1152 (2019).
3. Higashi, T., Friedman, S.L. & Hoshida, Y. Hepatic stellate cells as key target in liver fibrosis. Adv. Drug Deliv. Rev. **121**, 27–42 (2017).
4. Tsuchida, T. & Friedman, S.L. Mechanisms of hepatic stellate cell activation. Nat. Rev. Gastroenterol. Hepatol. **14**, 397–411 (2017).
5. Qiao, J.B. et al. Vitamin A-decorated biocompatible micelles for chemogene therapy of liver fibrosis. J. Control. Release **283**, 113–125 (2018).
6. Ji et al. Co-delivery of miR-29b and germacrone based on cyclic RGD-modified nanoparticles for liver fibrosis therapy. J Nanobiotechnology **18**, 86 (2020).

7. Tang, W. et al. Tandem Enzymatic Self-Assembly and Slow Release of Dexamethasone Enhances Its Antihepatic Fibrosis Effect. ACS Nano **12**, 9966–9973 (2018).
8. Schuppan, D., Ashfaq-Khan, M., Yang, A.T. & Kim, Y.O. Liver fibrosis: Direct antifibrotic agents and targeted therapies. Matrix Biol. **68–69**, 435–451 (2018).
9. Parola, M. & Pinzani, M. Liver fibrosis: Pathophysiology, pathogenetic targets and clinical issues. Mol. Asp. Med. **65**, 37–55 (2019).
10. Dunbar, C.E. et al. Gene therapy comes of age. Science **359**, eaan4672 (2018).
11. Cong, L. et al. Multiplex Genome Engineering Using CRISPR/Cas Systems. Science **339**, 819–823 (2013).
12. Ran, F.A. et al. Genome engineering using the CRISPR-Cas9 system. Nat. Protoc. **8**, 2281–2308 (2013).
13. Jinek, M. et al. A Programmable Dual-RNA-Guided DNA Endonuclease in Adaptive Bacterial Immunity. Science **337**, 816–821 (2012).
14. Lu, Y. et al. Safety and feasibility of CRISPR-edited T cells in patients with refractory non-small-cell lung cancer. Nat. Med. **26**, 732–740 (2020).
15. Yang, H. et al. One-Step Generation of Mice Carrying Reporter and Conditional Alleles by CRISPR/Cas-Mediated Genome Engineering. Cell **154**, 1370–1379 (2013).
16. Mout, R. et al. Direct Cytosolic Delivery of CRISPR/Cas9-Ribonucleoprotein for Efficient Gene Editing. ACS Nano **11**, 2452–2458 (2017).
17. Gong, J. et al. A Versatile Nonviral Delivery System for Multiplex Gene-Editing in the Liver. Adv. Mater. **32**, 2003537 (2020).
18. Thach, T.T. et al. Lipopeptide-Based Nanosome-Mediated Delivery of Hyperaccurate CRISPR/Cas9 Ribonucleoprotein for Gene Editing. Small **15**, 1903172 (2019).
19. Cheng, H., Zhang, F. & Ding, Y. CRISPR/Cas9 Delivery System Engineering for Genome Editing in Therapeutic Applications. Pharmaceutics **13**, 1649 (2021).
20. Chen, F.Q., Alphonse, M. & Liu, Q. Strategies for nonviral nanoparticle-based delivery of CRISPR/Cas9 therapeutics. Wiley Interdiscip. Rev.-Nanomed. Nanobiotechnol. **12**, e1609 (2020).
21. Sun, W.J. et al. Self-Assembled DNA Nanoclews for the Efficient Delivery of CRISPR-Cas9 for Genome Editing. Angew. Chem.-Int. Edit. **54**, 12029–12033 (2015).
22. Lee, K. et al. Nanoparticle delivery of Cas9 ribonucleoprotein and donor DNA in vivo induces homology-directed DNA repair. Nat. Biomed. Eng **1**, 889–901 (2017).
23. Alsaiari, S.K. et al. Endosomal Escape and Delivery of CRISPR/Cas9 Genome Editing Machinery Enabled by Nanoscale Zeolitic Imidazolate Framework. J. Am. Chem. Soc. **140**, 143–146 (2018).
24. Lee, Y.W. et al. In Vivo Editing of Macrophages through Systemic Delivery of CRISPR-Cas9-Ribonucleoprotein-Nanoparticle Nanoassemblies. Adv. Therap. **2**, 1900041 (2019).
25. Wei, T., Cheng, Q., Min, Y.L., Olson, E.N. & Siegwart, D.J. Systemic nanoparticle delivery of CRISPR-Cas9 ribonucleoproteins for effective tissue specific genome editing. Nat. Commun. **11**, 12 (2020).

26. Gao, X. et al. Treatment of autosomal dominant hearing loss by in vivo delivery of genome editing agents. Nature **553**, 217–221 (2018).
27. Mout, R., Ray, M., Lee, Y.W., Scaletti, F. & Rotello, V.M. In Vivo Delivery of CRISPR/Cas9 for Therapeutic Gene Editing: Progress and Challenges. Bioconjugate Chem. **28**, 880–884 (2017).
28. Carboni, V., Maaliki, C., Alyami, M., Alsaiari, S. & Khashab, N. Synthetic Vehicles for Encapsulation and Delivery of CRISPR/Cas9 Gene Editing Machinery. Adv. Therap. **2**, 1800085 (2019).
29. Rosenblum, D., Gutkin, A., Dammes, N. & Peer, D. Progress and challenges towards CRISPR/Cas clinical translation. Adv. Drug Deliv. Rev. **154**, 176–186 (2020).
30. Tian, K. et al. DNA and RNA editing without sequence limitation using the flap endonuclease 1 guided by hairpin DNA probes. Nucleic Acids Res. **48**, e117 (2020).
31. Tian, K. et al. AntiV-SGN: a universal antiviral strategy to combat both RNA and DNA viruses by destroying their nucleic acids without sequence limitation. Microb Biotechnol (2022).
32. Wu, P. et al. Efficient and targeted chemo-gene delivery with self-assembled fluoro-nanoparticles for liver fibrosis therapy and recurrence. Biomaterials **261**, 120311 (2020).
33. Li, Y. et al. An integrin-based nanoparticle that targets activated hepatic stellate cells and alleviates liver fibrosis. J Control Release **303**, 77–90 (2019).
34. Zhang, J.F. et al. Liver-Targeted siRNA Lipid Nanoparticles Treat Hepatic Cirrhosis by Dual Antifibrotic and Anti-inflammatory Activities. ACS Nano **14**, 6305–6322 (2020).
35. Luo, J. et al. Golgi Apparatus-Targeted Chondroitin-Modified Nanomicelles Suppress Hepatic Stellate Cell Activation for the Management of Liver Fibrosis. ACS Nano **13**, 3910–3923 (2019).
36. Luo, J., Zhang, Z., Zeng, Y., Dong, Y. & Ma, L. Co-encapsulation of collagenase type I and silibinin in chondroitin sulfate coated multilayered nanoparticles for targeted treatment of liver fibrosis. Carbohydr Polym **263**, 117964 (2021).
37. Qiao, J.B. et al. Hyperbranched lipoid-based lipid nanoparticles for bidirectional regulation of collagen accumulation in liver fibrosis. J Control Release **321**, 629–640 (2020).
38. Wu, J. et al. Synergistic MicroRNA Therapy in Liver Fibrotic Rat Using MRI-Visible Nanocarrier Targeting Hepatic Stellate Cells. Adv Sci (Weinh) **6**, 1801809 (2019).
39. Zhao, L.Z. et al. Fast-Clearable Nanocarriers Conducting Chemo/Photothermal Combination Therapy to Inhibit Recurrence of Malignant Tumors. Small **13**, 1700963 (2017).
40. Dam, D.H.M., Zhao, L.Z., Jelsma, S.A., Zhao, Y.L. & Paller, A.S. Folic acid functionalized hollow nanoparticles for selective photodynamic therapy of cutaneous squamous cell carcinoma. Mat. Chem. Front. **3**, 1113–1122 (2019).
41. Zhao, L.Z. et al. Independent of EPR Effect: A Smart Delivery Nanosystem for Tracking and Treatment of Nonvascularized Intra-Abdominal Metastases. Adv. Funct. Mater. **28**, 1806162 (2018).
42. Zhao, L.Z. et al. MTH1 inhibitor amplifies the lethality of reactive oxygen species to tumor in photodynamic therapy. Sci. Adv. **6**, eaaz0575 (2020).

43. Sung, Y.C. et al. Combined delivery of sorafenib and a MEK inhibitor using CXCR4-targeted nanoparticles reduces hepatic fibrosis and prevents tumor development. Theranostics **8**, 894–905 (2018).
44. Zhi, S.C. et al. Rosiglitazone Inhibits Activation of Hepatic Stellate Cells via Up-Regulating Micro-RNA-124-3p to Alleviate Hepatic Fibrosis. Dig. Dis. Sci. **64**, 1560–1570 (2019).
45. Wei, Z. et al. Rosiglitazone ameliorates bile duct ligation-induced liver fibrosis by down-regulating NF-kappa B-TNF-alpha signaling pathway in a PPAR gamma-dependent manner. Biochem. Biophys. Res. Commun. **519**, 854–860 (2019).
46. Wells, R.G. The role of matrix stiffness in regulating cell behavior. Hepatology **47**, 1394–1400 (2008).
47. Sander, J.D. et al. Selection-free zinc-finger-nuclease engineering by context-dependent assembly (CoDA). Nat. Methods **8**, 67-U94 (2011).
48. Joung, J.K. & Sander, J.D. INNOVATION TALENs: a widely applicable technology for targeted genome editing. Nat. Rev. Mol. Cell Biol. **14**, 49–55 (2013).
49. Jiang, W.Y., Bikard, D., Cox, D., Zhang, F. & Marraffini, L.A. RNA-guided editing of bacterial genomes using CRISPR-Cas systems. Nat. Biotechnol. **31**, 233–239 (2013).
50. Dominguez, A.A., Lim, W.A. & Qi, L.S. Beyond editing: repurposing CRISPR-Cas9 for precision genome regulation and interrogation. Nat. Rev. Mol. Cell Biol. **17**, 5–15 (2016).
51. Wang, H.X. et al. CRISPR/Cas9-Based Genome Editing for Disease Modeling and Therapy: Challenges and Opportunities for Nonviral Delivery. Chem. Rev. **117**, 9874–9906 (2017).
52. Yin, H., Kauffman, K.J. & Anderson, D.G. Delivery technologies for genome editing. Nat. Rev. Drug Discov. **16**, 387–399 (2017).
53. Li, J., Raise, J.J., He, M.M., Das, R. & Murthy, N. Non-viral strategies for delivering genome editing enzymes. Adv. Drug Deliv. Rev. **168**, 99–117 (2021).
54. Su, T. et al. Platelet-Inspired Nanocells for Targeted Heart Repair After Ischemia/Reperfusion Injury. Adv. Funct. Mater. **29**, 1803567 (2019).
55. Liu, C.H. et al. A multifunctional nanocarrier for efficient TRAIL-based gene therapy against hepatocellular carcinoma with desmoplasia in mice. Hepatology **67**, 899–913 (2018).
56. Li, N. et al. A mitochondria-targeted nanoradiosensitizer activating reactive oxygen species burst for enhanced radiation therapy. Chem. Sci. **9**, 3159–3164 (2018).
57. Frayne, S.H., Stolz, R.M. & Northrop, B.H. Dendritic architectures by orthogonal thiol-maleimide "click" and furan-maleimide dynamic covalent chemistries. Org Biomol Chem **17**, 7878–7883 (2019).

Figures

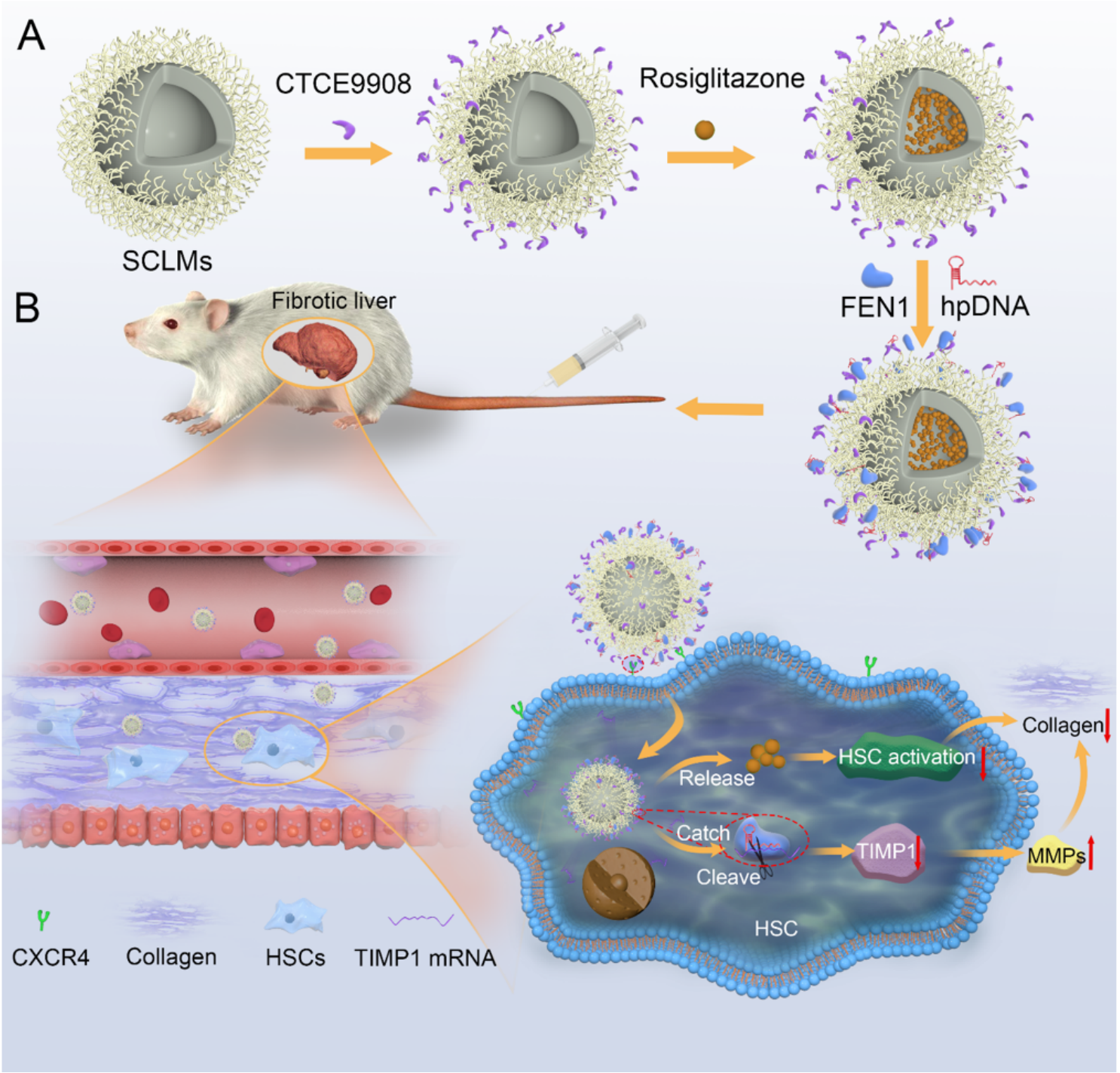

Figure 1

(A) Schematic illustration of the formation of the R@Hp-PSCLMs modified with CTCE9908 and HpSGN system (FEN1 plus hpDNA) loaded with rosiglitazone. (B) For the antifibrotic therapy in mice with fibrotic liver, the CTCE9908 on the intravenouly injected R@Hp-PSCLMs can bind to the overexpressed CXCR4 on activated HSCs, enhancing specific cellular uptake, whereupon the HpSGN system cleaved the mRNA for *TIMP1* to upregulate the MMPs for collagen degradation, and the released rosiglitazone suppressed the proliferation and activation of HSCs to inhibit the production of collagen.

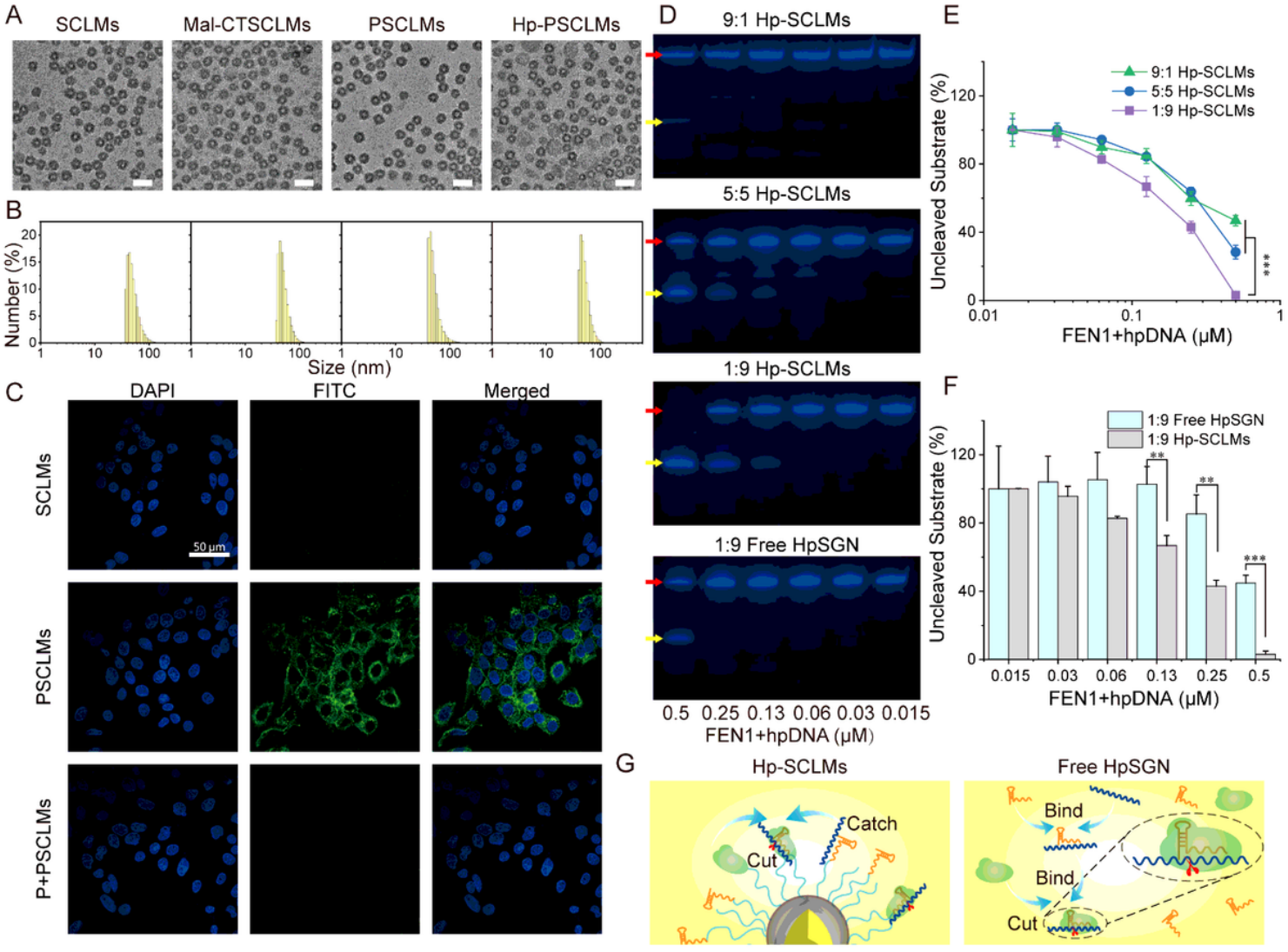

Figure 2

Characterizations of the nanocarriers and the *in vitro* ssRNA cleavage efficiency. (A) TEM images of SCLMs, Mal-SCLMs, PSCLMs and Hp-PSCLMs. Scale bar = 50 nm. (B) Hydrated size of SCLMs, Mal-SCLMs, PSCLMs and Hp-PSCLMs determined by DLS method. (C) The cellular uptake of FITC-modified SCLMs and PSCLMs by HSCs activated by TGF-β observed by CLSM. The nuclei of the HSCs were stained by DAPI. (D) PAGE results of the cleavage of ssRNA by Hp-SCLMs with different molar ratios of FEN1 to hpDNA at 9:1, 5:5 and 1:9. The cleavage of free HpSGN system with FEN1 to hpDNA ratio of 1:9 was also determined. The red arrow indicates the uncleaved ssRNA and the yellow arrow indicates the cleaved substrates. (E-F) Quantitative results of (D), the percentages of uncleaved ssRNA substrates in each group, data were analyzed by ImageJ (n = 3). (G) Schematic diagram of the accelerated gene editing efficiency by the Hp-SCLMs compared with free HpSGN system via the spatial confinement effect.

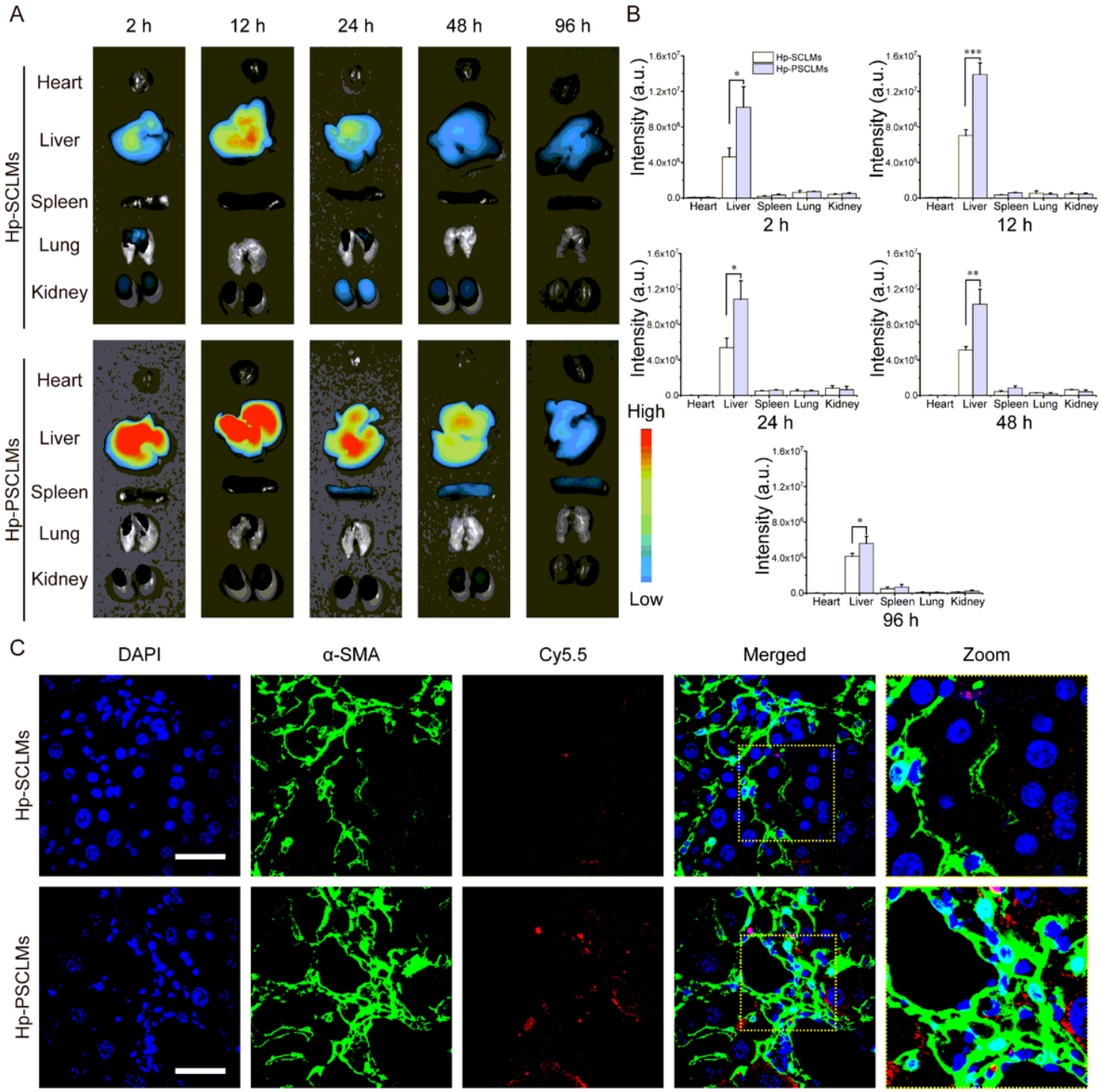

Figure 3

Biodistribution and intrahepatic distribution of Cy5.5-labelled Hp-SCLMs and Hp-PSCLMs i.v. injection. (A) *Ex vivo* imaging of the main organs (heart, liver, spleen, lung and kidney) of the fibrotic mice at 2, 12, 24, 48 and 96 h after the injection. (B) The integrated fluorescence intensity from the organs at 2, 12, 24, 48 and 96 h after the injection (n = 3). (C) Colocalization of the Hp-SCLMs and Hp-PSCLMs with α-SMA in the fibrotic liver. Blue, green, and red fluorescence indicate the DAPI-labelled nuclei, α-SMA, and Cy5.5-labeled nanoparticles, respectively. Scale bar = 50 μm.

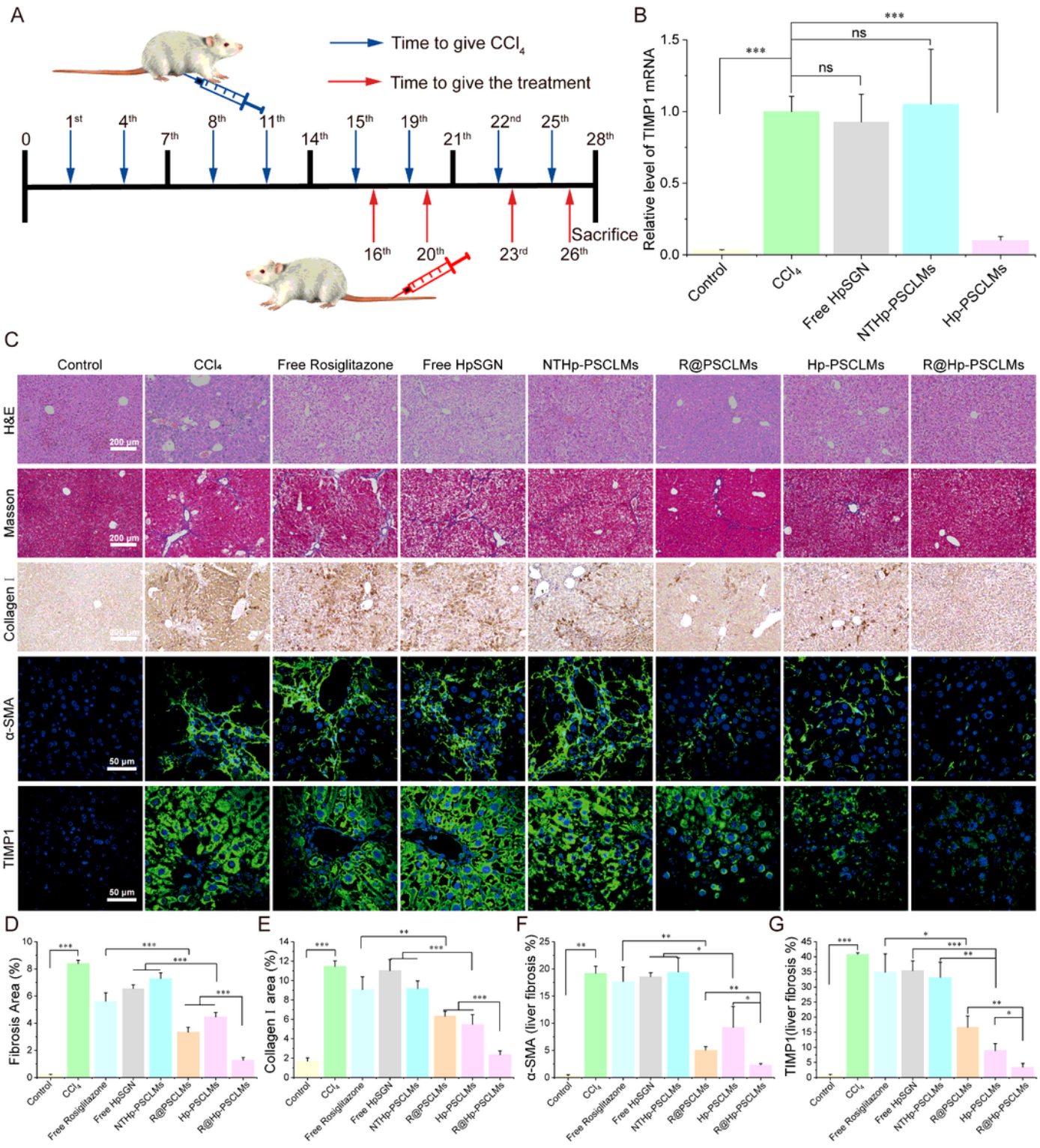

Figure 4

The nanomedicine R@Hp-PSCLMs with the payload of HpSGN system and rosiglitazone reversed the liver fibrosis. (A) Schematic diagram showing the modeling of the mice with fibrotic liver and the administration of the therapeutic in the treatment. (B) Real-time quantitative PCR analysis of the expression of *TIMP1* mRNA in the liver of the mice subjected to different treatments (n = 3). The effect of free HpSGN, NTHp-PSCLMs and Hp-PSCLMs were determined. (C) Representative images of the liver

sections stained by H&E, Masson trichrome staining, immunohistochemical staining of collagen I, α-SMA and TIMP1. The nuclei were counterstained with DAPI. Semi-quantitative analysis of the positive staining of the area of (D) Masson, (E) collagen I, (F) α-SMA and (G) TIMP1 staining sections by ImageJ (n = 5). The free drug, free HpSGN, NTHp-PSCLMs, R@PSCLMs and Hp-PSCLMs were used as negative control groups.

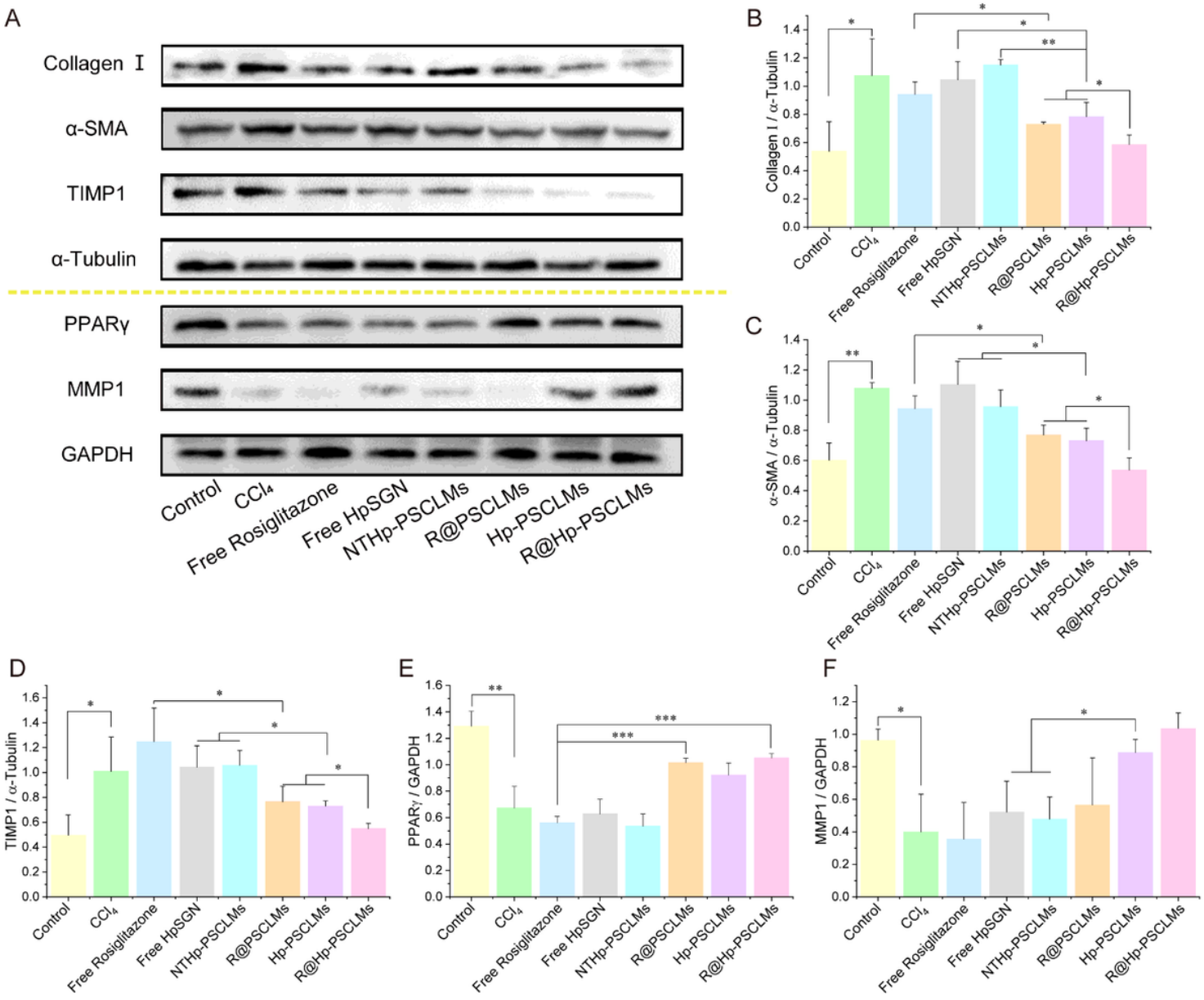

Figure 5

The influence of the chemogene therapy to the expression of the representative proteins involved in the liver fibrosis. (A) Western blot analysis of collagen I, α-SMA, TIMP-1, PPARγ and MMP1. Quantification of the protein bands of (B) collagen I, (C) α-SMA, (D)TIMP-1, using the α-Tubulin as the reference, and (E) PPARγ, (F) MMP1 using GADPH as the reference. The data were analyzed by ImageJ (n = 3).

Supplementary Files

This is a list of supplementary files associated with this preprint. Click to download.

- Supplementarymaterials.docx